Research Square

Preprints are preliminary reports that have not undergone peer review.
They should not be considered conclusive, used to inform clinical practice,
or referenced by the media as validated information.

Far field metal-enhanced luminescence nanothermometry

Beatriz Juarez

bh.juarez@csic.es

Instituto de Ciencia de Materiales de Madrid, ICMM https://orcid.org/0000-0003-1704-060X

Peijiang Wang

Instituto de Ciencia de Materiales de Madrid, ICMM

Daniel Carrica

Nanomaterials for BioImaging Group (nanoBIG).

Jaime Bueno

Instituto de Ciencia de Materiales de Madrid, ICMM https://orcid.org/0009-0000-1929-5783

Alejandro Hernández-Medel

Nanomaterials for BioImaging Group (nanoBIG)

Dirk Ortgies

Nanomaterials for BioImaging Group (nanoBIG) https://orcid.org/0000-0001-9693-6484

Manuel Rodriguez-Osorio

IMDEA-Nanociencia

Daniel Granados

IMDEA Nanociencia https://orcid.org/0000-0001-7708-9080

Celia Sousa

Nanomaterials for BioImaging Group (nanoBIG)

Carmen Munuera

Instituto de Ciencia de Materiales de Madrid https://orcid.org/0000-0001-8524-9304

Daniel Jaque

Universidad Autónoma de Madrid https://orcid.org/0000-0002-3225-0667

Alvaro Blanco

CSIC https://orcid.org/0000-0002-0015-4873

Sol Carretero Palacios

Emma Martín Rodriguez

Universidad Autónoma de Madrid https://orcid.org/0000-0002-2190-8312

Article

Keywords:

Posted Date: March 20th, 2026

DOI: https://doi.org/10.21203/rs.3.rs-8366629/v1

License: This work is licensed under a Creative Commons Attribution 4.0 International License.
Read Full License

Additional Declarations: There is **NO** Competing Interest.

Far field metal-enhanced luminescence nanothermometry

By P. Wang,[a⊥] D. Carrica, [b⊥] J. Bueno,[a⊥] A. Hernández-Medel,[b] D.H Ortgies,[,c,d,e,f] M. Rodríguez Osorio, [g] D. Granados,[g] Célia T. Sousa,[b,f] C. Munuera,[a] D. Jaque, [,c,d,e,f] A. Blanco, [a] S. Carretero-Palacios, [a] E. Martín Rodríguez,[b,d,e,f] B. H. Juárez [a] *

[⊥:] equal contribution

[a] *P. Wang, J. Bueno, C. Munuera, A. Blanco, S. Carretero,* ***B. H. Juárez****

Instituto de Ciencia de Materiales de Madrid, ICMM, Consejo Superior de Investigaciones Científicas, CSIC. Sor Juana Inés de la Cruz, 3, 28049 Madrid, Spain

E-mail: bh.juarez@csic.es

[b] *D. Carrica, A. Hernández-Medel, Célia T. Sousa, E. Martín Rodriguez*

Nanomaterials for BioImaging Group (nanoBIG), Departamento de Física Aplicada, Facultad de Ciencias, Universidad Autónoma de Madrid, C/ Francisco Tomás y Valiente 7, 28049, Madrid, Spain Madrid

D. H. Ortgies, D. Jaque

nanoBIG, Departamento de Física de Materiales, Facultad de Ciencias, Universidad Autónoma de Madrid, C/ Francisco Tomás y Valiente 7, 28049, Madrid, Spain

[d] *D. H. Ortgies, E. Martín Rodriguez, D. Jaque*

nanoBIG, Instituto Ramón y Cajal de Investigación Sanitaria (IRYCIS), Ctra. Colmenar Viejo, km. 9,100, 28034 Madrid, Spain.

[e] Institute for Advanced Research in Chemical Sciences (IAdChem), Universidad Autónoma de Madrid, 28049 Madrid, Spain

[f] Instituto de Ciencia de Materiales Nicolás Cabrera, Universidad Autónoma de Madrid, 28049 Madrid, Spain

[g] *M. Rodríguez Osorio, D. Granados*

IMDEA Nanoscience Foundation, C/ Faraday 9, Universidad Autónoma de Madrid, 28049 Madrid, Spain. Unidad de Nanomateriales Avanzados, IMDEA-Nanociencia, Unidad Asociada al CSIC por el ICMM. C/ Faraday 9, 28049 Madrid, Spain.

Abstract

Near-infrared (NIR) imaging and related sensing technologies must operate under biologically constrained conditions of low excitation power and strong tissue scattering, making efficient light extraction crucial. Here, we show that a simple architecture of Ag_2S-based nanoparticles deposited on metallic reflective surfaces markedly amplifies the photoluminescence (PL) signal through a mirror-induced optical feedback effect. This passive amplification enhances the signal-to-noise ratio (SNR) and allows detection through cm-thick tissue-mimicking media under low excitation power and short integration times. Furthermore, the increased SNR enables the temperature-dependent PL contrast to be quantified more reliably over the working temperature range, without modifying the intrinsic photophysical response of the emitters.

Integrating nanothermometers with metals as passive optical amplifiers thus provides a scalable route toward high-performance, bio-integrated photonic platforms for NIR imaging and thermometry, under realistic, tissue-relevant conditions

Introduction

Near-infrared (NIR) emitters are essential components in the development in a wide range of biomedical imaging and sensing technologies, from fluorescence-guided surgery to minimally invasive biosensing.[1] For NIR imaging, in particular, their impact ultimately depends on how efficiently their emission can be detected in complex, turbid media, and collected through highly scattering and absorbing tissues, under clinically acceptable excitation conditions.[2] Among the various implementations of NIR sensing, Luminescence Nanothermometry (LNT) [3,4,5] is specially demanding, as it requires the accurate quantification of temperature-dependent photoluminescence-related signals under exactly those biologically-constrained conditions. LNT has been applied *in vivo* in mice models,[6] to early detect solid tumors,[7] ischemic events,[8] and hepatic disorders.[9] Among NIR fluorophores,[1] Ag_2S-based nanoparticles are particularly attractive NIR emitters owing to their low toxicity, favorable spectral window and chemical versatility, having used previously for NIR imaging and LNT pourposes.[10] Together with synthetic approaches that incrementally improve the photoluminescent quantum yield (PLQY) of these

probes, [11,12] deep learning frameworks to extract reliable information from deep tissues have been recently applied.[13,14] In this context, computational advances must be complemented by strategies that optimize fluorophore emission and signal collection.

In this study, we present *proof-of-concept* studies combining Ag_2S-based NPs with metallic surfaces to increase the photoluminescence (PL) response. We show that optical architectures specifically tailored to boost collection efficiency and signal robustness can be as critical as the chemical optimisation of the nanothermometer. This complementary design route markedly strengthens the detected NIR signal and, in turn, enhances the reliability of temperature readout through tissue-mimicking media.

From the pioneering work of Purcell[15,16] and Drexhage,[17] it is well established that metals can strongly modify the emission dynamics of nearby fluorophores. Depending on the distance between the fluorophore and the metal surface, two distinct regimes emerge: near-field and far-field. In the near-field regime, localized surface plasmons (LSPs) and surface plasmon polaritons (SPPs) propagating at the metal-dielectric interface have been extensively exploited to study strong or weak light-matter coupling phenomena, control the local density of optical states, and enhance fluorescence emission through near-field electromagnetic confinement.[18,19,20,21] Such effects have been demonstrated in a wide variety of emitters, ranging from organic molecules to semiconductor NPs, including colloidal quantum dots and UCNPs. [22,23,19,24] Indeed, numerous luminescent biological sensors rely on the well-established metal-enhanced fluorescence (MEF) effect, which has proven valuable in biosensing,[25] imaging,[26] and analytical applications.[27]

In the far-field regime, when fluorophores are placed sufficiently far from metallic surfaces to avoid significant near-field plasmonic coupling (hundreds of nanometers or micrometers), the dominant enhancement mechanisms arise from optical interference and/or reflection effects rather than from localized electromagnetic coupling. In this context, mirror reflection, interference, cavity resonances, or photonic mode engineering can be exploited to increase the detectable luminescence signal, improve emission directionality, and modulate the optical path length of the emitted light.[28,29,30] These mechanisms can substantially enhance the collected PL intensity without relying on the near-field plasmonic coupling that governs the MEF effect. For instance,

enhanced PL cell imaging has been demonstrated using metal-coated slides,[26] while mirror-enhanced fluorescence techniques, such as super-resolution microscopy employing metal/dielectric mirror stacks have also exploited these effects to boost signal brightness.[31,32] In the far-field regime, dielectric spacer layers with thicknesses ranging from tens to hundreds of nanometers are typically used to suppress near-field plasmonic effects, ensuring that constructive interference and optimized PL collection dominate.[33,30,34]

In this study, we demonstrate that even a simple metal-backed architecture can significantly enhance the PL of micrometer-thick Ag_2S-based NP layers via reflection-assisted light extraction. Time-resolved PL measurements revealed unchanged lifetimes on metallic and silicon substrates, confirming that the intrinsic radiative and non-radiative rates remained unaffected. Supported by optical simulations, these results establish that the observed enhancement arises from substrate-mediated outcoupling and mirror reflection, which redirects the emitted photons toward the detector without altering the emitter dynamics. The enhanced signal-to-noise ratio (SNR) allows for a temperature-dependent contrast that can be quantified more reliably over the working-temperature window. This translates into more reliable temperature readouts under low-power excitation, short integration times, and centimeter-scale tissue-mimicking depths, bringing the experimental conditions closer to those required for realistic, practical biomedical applications. Indeed, reliable PL signals were obtained at depths of 1.5 cm within highly scattering tissue-mimicking phantoms at an irradiance as low as 15.8 mW/cm^2 and 90 ms integration times, highlighting the potential of this approach for deep-tissue thermal imaging.

These results pave the way for the development of novel metal-fluorophore architectures and photonic device structures that exploit mirror-assisted enhancement to improve subcutaneous NIR imaging and thermometric response. In particular, these concepts can be extended toward labelling metallic probes for thermal therapies, encoding implants, or guiding X-ray–visible devices with an additional NIR optical channel.

Results and discussion

The Ag_2S-based NPs used in this study were synthesized using two different synthetic routes, known as *the heat-up* and *hot-injection methods* (see Supporting Information (SI) for details). Representative images of these NPs are shown in the Transmission Electron Microscopy (TEM) images in **Figures 1a-c**. Following the *heat-up* methodology Ag_2S NPs (hereafter referred as Ag_2S HU NPs) are produced by thermal decomposition of a silver salt (silver(I) diethyldithiocarbamate).[35,36] This reaction yields hexagonal micrometric NPs-assemblies (see **Figure 1a**), arising from the formation of a silver(I) dodecanethiolate, a byproduct formed during the thermal decomposition that acts a template where the NPs nucleate and grow, as previously reported.[37] In contrast, the *hot-injection*-approach produces individual Ag_2S NPs that grow without templating, free of silver(I) dodecanethiolate, enabling post-synthetic Se and Zn treatments. These post-treatments substantially improved the photoluminescence quantum yield (PLQY) from below 1% for the initial Ag_2S NP-cores to 10% as a result of better surface passivation.[38] Treatment with Se yielded $Ag_2S/Ag_2(S,Se)$ NPs (hereafter named CS NPs), while sequential treatment with extra Zn produced $Ag_2S/Ag_2(S,Se)/ZnS$ NPs (referred to as CSS NPs).

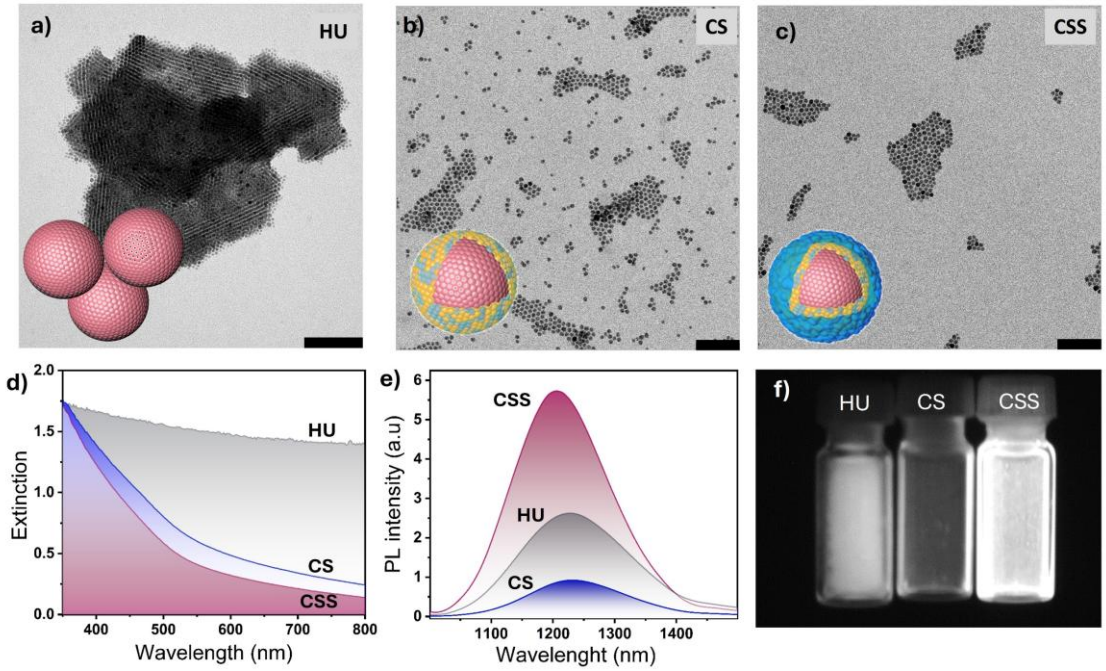


Figure 1. *TEM images of (a) Ag_2S NP arrangements produced by heat-up (HU NPs), (b) Ag_2S individual NPs produced by hot injection treated with Se (CS NPs) and (c) and Ag_2S individual NPs produced by hot injection treated with Se and Zn (CSS NPs). Scale bars: 100 nm. d) Extinction response of Ag_2S-based NPs. e) PL spectra. f) NIR PL image of the Ag_2S-NP solutions showing increased brightness from CS to HU and CSS NPs.*

Representative TEM images of CS and CSS are shown in **Figures 1b-1c**. The steady-state optical properties of all three samples (HU, CS, and CSS) are gathered in the spectra shown in **Figure 1d**. In the left panel, the extinction spectrum of the HU NPs (gray line) differs markedly from that of the hot injection samples, primarily because of the pronounced light scattering in the visible region arising from the micrometer-sized NPs assemblies. As previously reported,[36] the size of these assemblies can be controlled by sonication in chloroform from approximately 500 to 70 nm. The HU sample used in this work corresponds to larger assemblies with an average size of approximately 500 nm. The PL emission properties in **Figure 1e** show a comparative response for similar diluted NP solutions. As is clearly seen, colloidal HU NPs exhibit an intermediate PL intensity response, lying between that of CS and CSS NPs.

The observed trend in the PL intensities follows the expected behavior based on previously reported PLQY values: 2.6% for HU NPs produced by heat-up,[37] ~1% for individual CS NPs,[37] and ~10% for CSS NPs.[38] Although scattering may play a minor role, the higher PLQY of HU compared to CS is attributed to their higher crystallinity resulting from the higher synthesis temperature (200 °C for HU and 100 °C for CS NPs). The optical spectra in **Figure 1e** corroborate this behavior.

Optical wells

To investigate the influence of the metal substrate on the Ag_2S-based NPs, wells were photolithographically fabricated on silicon wafers (**Figure 2a**). These wells consisted of sets of cylindrical cavities with circular cross sections, 1 mm or 2 mm in diameter and 17 or 40 μm deep, separated by 500 μm (**Figure 2b**). The bottom surfaces of the wells were coated with a 100 nm metal layer (either a 10 nm Cr adhesion layer followed by 90 nm of Au or a single 100 nm layer of Ag), allowing direct comparison with uncoated Si wells. The profilometric profiles of the 17 μm (2 mm in diameter) and 40 μm (1 mm in diameter) wells are shown in *Figure S1*, in the SI. **Figure 2c** schematically illustrates the deposits obtained by drop-casting concentrated NPs solutions when they are placed on top of these wells.

The low volume and high initial concentration of the colloidal solutions (2 µL at ~18.5 mg/mL), along with the shape and depth of the wells, facilitated the formation of reasonably homogeneous deposits, thereby avoiding the coffee-stain effect. In any case, the different drying behaviors of the solutions resulted in unavoidable imperfect deposits and packing tendencies. To illustrate these issues, *Figures S2–S4*, SI, show FESEM images of the surface of the deposits at different magnifications. Local inhomogeneities and partial spreading of NPs outside the well boundaries in micrometric areas were observed (*Figure S2*). Field Emission Scanning Electron Microscopy (FESEM) images revealed that the CS samples exhibited the most compact arrangement, with packing densities approaching the theoretical maximum filling fraction for equal spheres in three dimensions (74%) (see *Figure S3-S4*). The HU samples also formed dense deposits but displayed microcracks and slightly lower filling fractions of approximately 70%. In contrast, the CSS samples showed markedly looser and irregular assemblies, with estimated filling fractions

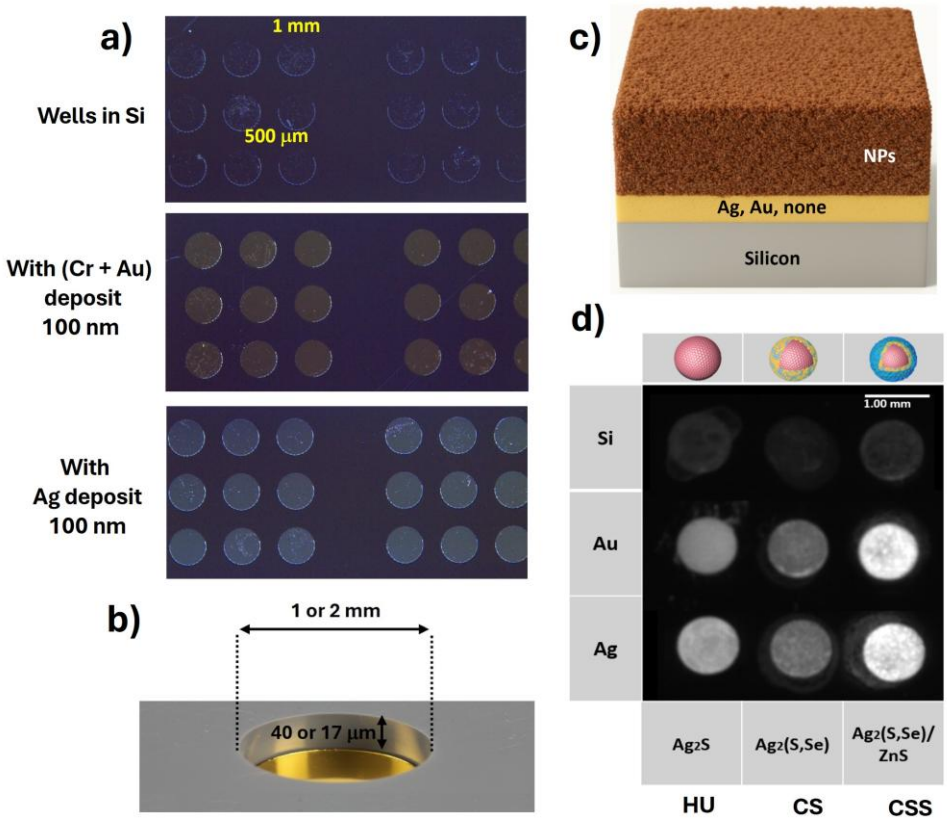


Figure 2. *a) Optical images of photolithography-fabricated wells in bare silicon (top), silicon covered with Au (middle), and Ag (bottom) films. b) Schematic of the well geometry and size. c) Image depicting NPs deposits on the surface of the wells. d) NIR images acquired using an NIR hyperspectral imaging setup under an 808 nm laser at 0.69 W (irradiance of 15.8 mW/cm^2).*

between 60% and 40%. This packing behavior remained consistent across all substrates (as evidenced in *Figure S5*), indicating that ligand chemistry, rather than substrate composition, plays a major role in the drying and arrangement processes.

NIR images and corresponding spectra of the deposits were acquired with an NIR hyperspectral setup, allowing for both imaging and spectroscopic information (see *SI* for details). The NIR image shown in **Figure 2d** shows that the metallic substrates (Au and Ag) greatly modified the brightness of the NP deposits with respect to that obtained on Si. Importantly, the limitations of drop casting do not affect the general trend observed. Further NIR images from deposits with different NP solutions and on 1 mm and 2 mm diameter wells can be found in *Figure S6*, SI.

PL characterization. Decay dynamics

Figures 3a-c show the PL intensity values obtained from each image of the wells shown in Figure 2d for HU, CS, and CSS NPs. In all cases, a clear PL enhancement was evident, regardless of the NPs type, when placed in metallic wells. The PL enhancement corresponds to 3.6x times in the case of HU and CS NPs, and 4.8x for the CSS. To understand whether the metals modify the radiative decay rates, the PL decay dynamics were measured using a 643.3 nm laser focused on each well with a 5 μs repetition period (further details are provided in the *SI*). **Figures 3d-3f** show the normalized PL decay curves for the HU, CS, and CSS NPs in the Si, Ag, and Au wells, where only slight and non-representative modifications in the relaxation dynamics can be observed. Comparison among four mathematical models (mono exponential, bi-exponential, tri-exponential and log-normal distribution, see *SI*) demonstrate an optimum fitting to bi-exponential functions, consistent with previous characterizations in colloidal solutions.[38] The bi-exponential model accounts for a distribution of recombination pathways with different degrees of trap involvement. The faster contribution can be associated with NPs strongly affected by nonradiative trap-related quenching (often surface-related), whereas the slower contribution reflects radiative recombination from Ag_2S nanocrystals with fewer quenching centers.[39] Recently, it has been reported that biexponential fit should not be interpreted as evidence for only two distinct emissive species, but rather as a convenient parameterization of an intrinsically multiexponential

decay.[40] ***Table 1****, SI* indicates that the substrate material (Si, Au, Ag) exerts minimal influence on PL dynamics. Averaging across the three types of NPs yields mean lifetimes of 258 ns (HU), 324 ns (Au), and 888 ns (CSS), values in good agreement with those measured previously for NPs in colloidal solutions,[38] a remarkable result that demonstrates the effectiveness of the organic passivating layer against oxidation (the wells were exposed to air for months). Thus, PL kinetics are governed primarily by the surface electronic states rather than by substrate-mediated effects, such as plasmonic enhancement or charge transfer. The absence of significant changes in the PL decay dynamics further indicates that the observed PL enhancement may result predominantly from far-field optical effects rather than near-field plasmonic coupling, which would modify radiative pathways upon excitation. In other words, our results indicate that radiative decays are minimally affected by local field enhancement, suggesting that the improved light extraction is primarily related to the reflected light being redirected back into the collection optics.

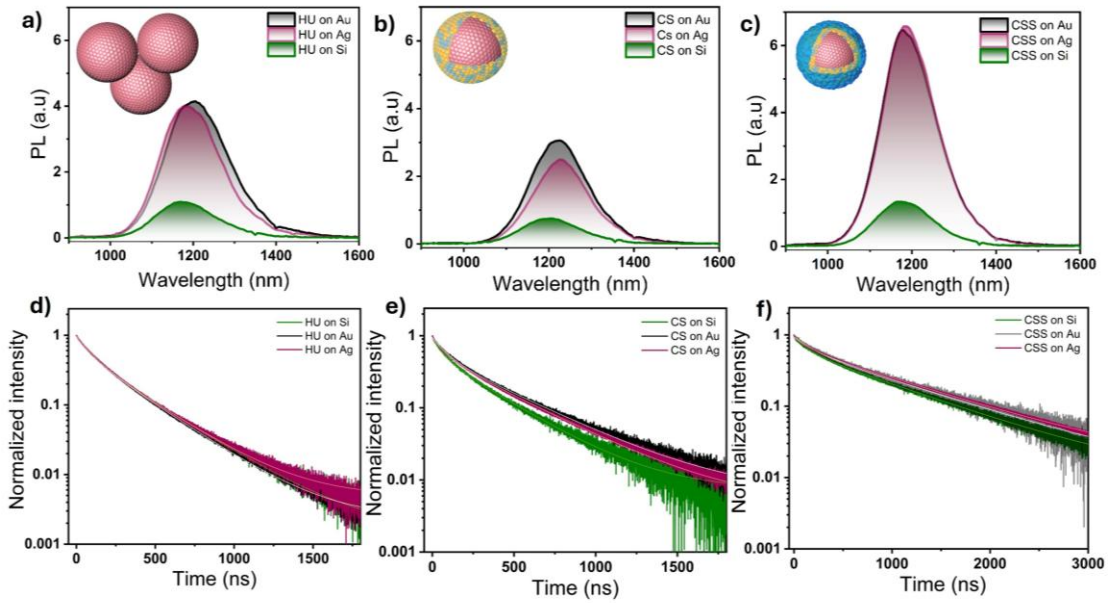


Figure 3. *PL spectra for Ag_2S a) HU, b) CS, and c) CSS NPs on Silicon (black), Au (red), and Ag (purple), where an evident PL increase is observed for NPs placed on the metallic wells, regardless their composition. Corresponding decay dynamics and fitting of the bi-exponential functions of d) HU, e) CS, and f) CSS.*

Surface potential measurements

To gain deeper insight into the effect of the metallic substrates on the electronic properties of the NPs, and to rule out plasmonic effects, we performed Kelvin probe force microscopy (KPFM) measurements on both empty and NP-filled wells. The local electronic properties of HU Ag_2S NPs on different substrates were investigated, providing correlated topographic and surface potential maps. KPFM is inherently sensitive to the local electrostatic potential at the sample surface, which reflects variations in the work function, surface charges, and band alignment between the tip and sample.[41] In this study, if near-field electromagnetic confinement or localized magnetic coupling played a dominant role, significant differences in SP were expected between the substrates. **Figures 4** shows simultaneous topographic and surface potential (SP) images of empty and filled wells with HU Ag_2S NPs. Triangular aggregates were observed, and their morphology was in good agreement with that observed in the FESEM images depicted in *Figure S3*, SI. A visual comparison of the SP maps adjusted to the same color scale clearly revealed an increase in the SP of the NP-filled wells. As shown in the lower panels of Figure 4, the empty

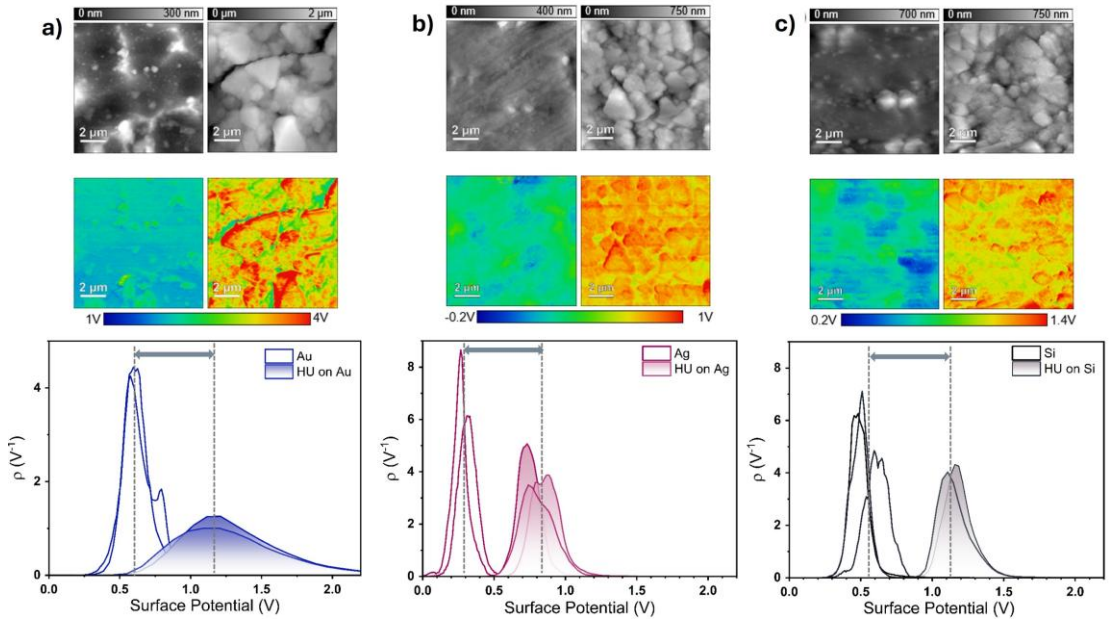


***Figure 4**.-KPFM measurements performed on the Au (a), Ag (b), and Si (c) wells comparing the empty and HU NP filled surfaces. The top row displays representative topographic images, and the middle row shows the corresponding surface potential (SP) maps. The bottom panels show the surface potential histograms extracted from the corresponding maps. In all cases, a clear distinction in SP was observed between the empty and NP-filled wells, with the distributions showing well-clustered values obtained from sequential, alternating measurements, confirming the high reproducibility of the results.*

wells already exhibit noticeable variations in SP, reflecting the intrinsic differences in the work function of the underlying materials (see *Figure S7, SI* for comparative SP of the different substrates). Upon deposition of the HU Ag_2S NPs (as a representative sample), an increase in SP was observed for all substrates, regardless of the substrate material. The increase was approximately 0.6 V for all samples, as exemplified by the arrow covering the rough SP difference between the empty and filled wells. The larger SP distribution on Au can be attributed to its rougher morphology. In our KPFM configuration (with a bias applied to the tip), higher SP values correspond to more negatively charged surfaces. Accordingly, the SP enhancement observed in the NP-filled wells can be attributed to an increased electron density compared to that in the empty wells.

The increasing trend and magnitude of the SP in all cases (~0.6 V), including bare Si, indicate that the substrate does not play a dominant role in modulating the SP of the NPs. Instead, the measured SP reflects an intrinsic electrostatic/electronic property of the NPs assemblies, which is sensitive to band alignment and long-range Coulombic effects at the micrometer scale. The magnitude of the observed SP values is strongly influenced by the inherent features of the micrometer-thick NP films, such as packing density and capping ligands, where trap states, surface charges, and grain boundaries give rise to internal electric fields and space-charge regions within the deposits. In other words, our results suggest that the influence of the substrate is effectively screened by the thick NP layers, and that the observed PL enhancement is not governed by the electromagnetic nature of the underlying metal

Far-field optics calculations

To gain deeper insight into the origin of the observed PL enhancement, we performed optical simulations using the transfer-matrix method (TMM).[42] The structure was modeled as a planar multilayer stack (air/Ag_2S (17 μm) / metal (100 nm) / Si), as shown in Figure 2c. The refractive indices used in the simulations were taken from literature values for bulk Ag_2S,[43] from Johnson and Christy data for metals,[44] and from Palik for crystalline silicon.[45]

To reproduce the morphology observed experimentally by FESEM (see *Figure S3-S5,* SI), the NP layer was treated as an effective homogeneous medium whose refractive index was calculated using a Bruggeman effective-medium approximation to account for porosity.[46] Equivalent trends were obtained using a simple volumetric mixing model (*Figure S8, SI*), confirming the robustness of this approach. The packing fractions were chosen to match the observed morphologies: ~74% for CS samples with ordered packing, ~70% for HU samples exhibiting partial aggregation, and ~40% for CSS samples displaying a more random, porous arrangement. Additional simulations for more densely packed CSS layers (up to 60% filling fraction) are provided in *Figure S9, SI*

The simulations were performed in two steps. First, the system was illuminated with a plane wave at λ = 808 nm under normal incidence, and the spatial distribution of optical absorption within the NP layer was determined to identify the region from which the emission originated. Second, the emission from the Ag_2S NPs was modeled as radiation from isotropic dipole emitters uniformly distributed along the z-axis (depth direction) within the Ag_2S layer, which was assumed to be optically transparent at the emission wavelengths. The emission spectra were weighted using the measured PL of the colloidal Ag_2S NP solutions (Figure 1e) and modulated by the computed excitation field distribution, ensuring realistic spectral and spatial weightings. The total power radiated into the far field was integrated over all the emission angles to estimate the detected PL intensity.

In this model, the internal PLQY was kept constant, as the emitter-metal separation (>100 nm) is too large for any significant modification of the local density of optical states (LDOS) or Purcell enhancement (see *Figure S10, SI*).[47] Nevertheless, for emitters located much closer to the metal, enhanced radiative recombination could drive the PLQY toward unity.[48] Simulations of PL enhancement across different substrates were then performed using experimental PLQY values of 2.5%, 1%, and 9% for HU, CS, and CSS NPs, respectively, according to previous reported studies.[37,38]

To emulate the experimental films, which lack perfectly plane-parallel interfaces, the calculated spectra were smoothed to average out the fine interference fringes, effectively mimicking random-phase averaging and suppressing coherent interference effects (see *SI* for details). Other possible

contributions, such as reabsorption or photon recycling, were neglected because of the large Stokes shift of the Ag_2S emission (see Figures 1d-e).

Figure 5a shows a contour map of the excitation and emission profiles of the Ag-backed substrate. The profile indicates that even for the most porous case (40% filling fraction, corresponding to CSS NPs), the excitation remains confined to the topmost ~3 μm and does not directly reach the metal interface (**Figure 5b**). This excitation depth arises from the average optical field intensity computed by the TMM under incoherent conditions, where absorption and reflection dominate over interference or Beer-Lambert-type attenuation.

The simulations account for both emissions that exit directly toward the collection optics and emissions that are initially directed laterally or downward and are then reflected upward. Photons impinging on the metal interface are efficiently redirected into the upper half-space, thereby increasing their probability of scaping through the top surface. Because Ag and Au exhibit NIR reflectivities approximately three times higher than that of Si, the experimentally observed PL enhancements of ≈3.6× and ≈4.8x for different NP types can be mostly explained by this mirror-assisted light-extraction mechanism, without invoking any plasmonic effects.

Following the experimental trend, the absolute PL intensity obtained from the TMM simulations (**Figures 5c–e**), based on an effective homogeneous medium without explicit scattering, increased inversely with packing density (CSS > HU > CS), consistent with the lower effective refractive indices and improved optical coupling predicted for less dense layers. However, the calculated enhancement factor between the metals and Si remained nearly constant (≈2.3×) for all NP types and lower than the experimentally attained values. This constancy explicitly reflects that, within the effective-medium model, the relative PL enhancement between the metallic and Si substrates is mainly governed by their reflectivity contrast, whereas the absolute PL intensity still depends strongly on the effective refractive index of the Ag_2S layer.

Experimentally, in contrast, the relative PL enhancement (metal *vs.* Si) follows the trend CS ≈ HU < CSS, with enhancement factors of approximately 3.6×, 3.6×, and 4.8×, respectively. This deviation from the nearly constant enhancement predicted by the TMM model indicates that additional structural and optical factors, such as scattering and variations in the effective refractive

index, influence the experimental results. In particular, the fact that the simulated enhancement is not only constant but also systematically smaller than the measured one arises because the TMM description cannot capture angular redistribution of light or depth-dependent refractive-index gradients, both of which significantly improve outcoupling in the real, porous NP assemblies.

The simulations employed the refractive index of bulk Ag_2S reported in the literature, whereas real NP assemblies possess lower effective indices owing to porosity or the presence of surface ligands. A smaller effective refractive index reduces the Fresnel losses at the air interface and enhances light extraction, which is consistent with the stronger PL observed for the more porous CSS films. Moreover, as previously mentioned, the packing density within the NP layers is likely not homogeneous across the thickness or identical among different substrates, leading to depth-dependent effective refractive indices that are not considered in the model. Such spatial gradients can modify the optical path of both excitation and reflected photons, slightly altering the efficiency of the mirror-reflected light decoupling toward the detector.

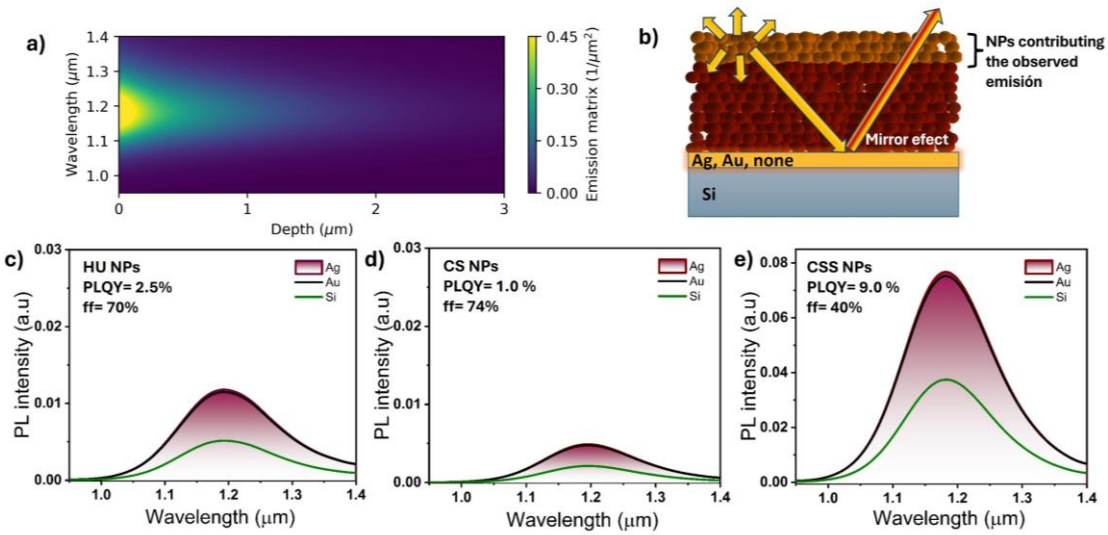


Figure 5 *a) Contour map of the excitation-emission process for a plane wave incident on wells containing a 17 μm-thick Ag_2S layer (CSS-type NPs) deposited on a semi-infinite Si substrate, modeled using the Bruggeman effective-medium approximation for the NP refractive index. Simulations were performed at λ = 808 nm under normal incidence; the color scale represents the normalized electric-field intensity escaping the system. b) Schematic representation of the NP layers on the substrate, illustrating that only the upper few micrometers are optically excited and contribute to the detected PL. c–d) Simulated PL enhancement factors for HU, CS, and CSS NPs, calculated assuming PLQY values of 2.5 %, 1 %, and 9 %, respectively. The filling fractions were chosen according to the morphologies observed in the FESEM images: 74 % for HU, 70 % for CS, and 40 % for CSS samples*

In addition, in the experimental samples, the porous and structurally disordered nature of the Ag_2S NP layers inevitably introduces light scattering. This scattering redistributes the photon trajectories inside the film and can locally increase the optical path length by redirecting the photons multiple times within the NP layer. On the one hand, photons undergoing multiple scattering events might be reabsorbed within the upper few micrometers of the film, well before they reach the metal substrate below, without experiencing the reflectance enhancement. On the other hand, light scattering also allows part of the emission that would otherwise remain trapped by total internal reflection or guided modes to couple through the air interface, providing higher outcoupling to the emitted signal. This could explain why the experimental scattered layers exhibit more efficient light extraction and slightly higher apparent PL intensities than the calculated ones. The relative experimental enhancement across different metals observed for more porous samples likely reflects additional outcoupling channels enabled by structural scattering, an effect inherently absent in the planar TMM approximation, in which the emission is specular and the photons emitted beyond the critical angle remain confined within the high-index medium, leading to a lower predicted extraction efficiency. Consequently, scattering enhances the outcoupling efficiency but does not increase the depth of the optically active region predicted by the simulations. Overall, these results confirm that the dominant mechanism of PL amplification is substrate-mediated light extraction, where isotropically emitted photons from the optically active upper ~2-3 μm of the NP layer are reflected by the underlying metal and redirected toward the detector. Thus, the metal acts mostly as an optical mirror that enhances the detected PL intensity without altering the intrinsic radiative or nonradiative rates of the emitters.

Thermal response

To evaluate the thermal response of the wells, three sets of wells (Si, Ag, Au) containing different Ag_2S-based NPs were placed on a heating plate, and the temperature was simultaneously recorded using a thermal camera in the range of 30-60°C. Some wells were loaded with HU, some with CS, and some with CSS NPs, as previously described in Figure 2 and in the *SI* section. **Figures 6a** shows the thermal images of the three sets of wells: Those of bare Si, and those covered with

Au and Ag at 30.7 °C (top figure) and 57.3 °C (bottom image). The different colors observed for wells on Si and those with metals are caused by the well-known low emissivity of metals, which reflect ambient IR radiation instead of emitting their own signal. This caused an underestimation of the surface temperature, which is why metals appeared colder in the thermal images. Therefore, only the temperature values of the silicon wells were considered. The vis and thermal images at different temperatures from 30.7 °C to 57.3 °C are shown in *Figure S11* and *S12* in SI, respectively. **Figure 6b** shows the NIR images at 30.7 °C (top) and 57.3 °C (bottom). The different brightness of the spots is related to the different PLQY values of the NPs loaded on them. Thus, the spots with lower intensity corresponded to wells loaded with CS NPs (with a PLQY of less than around 1%), the spots with an intermediate brightness with HU NPs (with a PLQY of 2.6 %), and the brightest spots corresponded to wells loaded with CSS NPs (with a PLQY close to 10%). A complete map of each sample is shown in *Figure S11*, SI. Direct comparison of the top and bottom NIR images, evidence that, while all spots are visible at the lowest T (30.7°C), only some of them are clearly discernible at temperatures closer to 60 °C, and especially those deposited on the metallic wells.

Figures 6c shows the PL trend with T of the different NPs (HU, CS, and CSS) in the corresponding wells (Si, Ag, and Au) when varying the T from 30.7 to 57.1 °C in steps of ~5 °C.

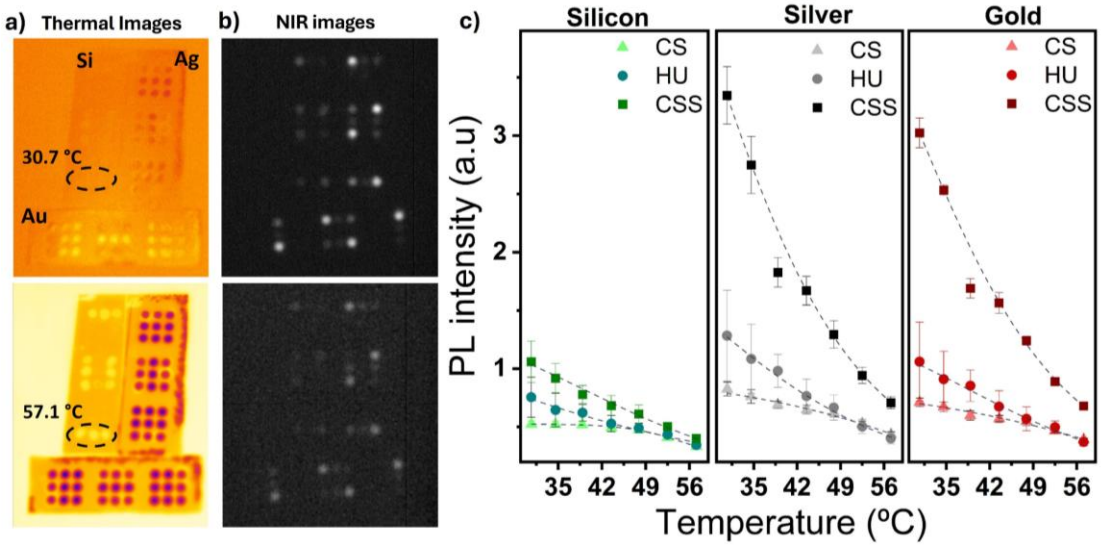


***Figure 6**. Thermal (a) and NIR (b) images of wells on bare Si and wells with Ag and Au loaded with Ag_2S-based NPs. c) PL intensity versus temperature for CS (triangles), HU (dots), and CSS NPs (squares) on silicon (left), silver (middle), and gold substrates (right) panels.*

In the three panels, the less intense data (triangles) correspond to CS NPs, the intermediate-intensity data correspond to HU NPs (dots), and the highest-intensity data (dark squares) correspond to CSS NPs. As it can be seen, the PL obtained on Ag and Au (middle and right panels, respectively) markedly increased with respect to those acquired on Si (left panel), in good agreement with the brighter NIR images shown in Figure 6b, regardless of the type of NPs (HU, CS, or CSS).

The error bars correspond to the standard deviation calculated from four replicate wells of each type prepared on three different substrates, (see SI for further information). The dashed lines for Ag and Au (middle and right panels) correspond to the fitting of the points (except for 38.8 °C for CSS NPs) to an Arrhenius function, and only as guides for the eye. As it can be seen, the impact of its optical amplification seems to be more pronounced at lower temperatures, where the PL of the emitter is stronger. Far from a modulation of the outcoupling efficiency at different temperatures, this can be simply related to a lower SNR at higher temperatures, which makes the dependence more difficult to measure. This effect can be better observed in *Figure S13*, SI where, instead of the average PL of four wells, the PL intensity variation within selected wells is plotted. Above 50 °C, the SNR is low and the corresponding data are therefore less reliable. It should be emphasized, however, that temperatures up to ~45 °C already cover the most relevant biomedical regimes and temperatures beyond this threshold are of limited practical interest. Thus, within the biomedical range, the mirror-induced amplification is clearly observed and the signals remain extremely robust.

NIR imaging

As shown above, the NPs can be efficiently excited by an 808 nm laser, a wavelength located in the first biological window that is commonly used for deep-NIR imaging and LNT. To assess the potential of NP substrates for deep-tissue NIR imaging and nanothermometry, we performed an NIR imaging *proof-of-concept* study. **Figures 7a-b** show the setup: An agar phantom (2.2 cm in diameter, 1.5 cm thick, containing 1% intralipids, see *SI*) was placed on top of wells filled with NPs deposited on Si, Au, or Ag substrates. Images acquired under direct 808 nm excitation laser

at 15.8 mW/cm^2 (well below the value of 50 mW/cm^2 irradiance used for *in vivo* experimentation) were compared with those obtained with the scattering phantom on top, mimicking thick tissue. The agar scatters highly, as it contains 1% (v/v) of intralipids (preparation and details in *SI*). As can be seen by comparing the first column of the NIR images in Figure 7, the wells with no phantom on top can be recorded at very low integration times (0.5 ms). The best performance was obtained for samples on Ag, where the highest brightness was observed.

Well-resolved and individual wells are clearly discernible for the sample acquired at an integration time of 1s (indicated by yellow arrows for the case of Ag). The green arrow in the top row indicates an artifact. The results are particularly noteworthy, given the low excitation irradiance and strong optical scattering of the 1.5 cm-thick medium. Despite these challenging conditions, a clear signal was obtained with an integration time of only 90 ms, demonstrating the potential of this approach for applications that require high temporal resolution.

This is especially relevant for live-cell imaging, where temperature variations associated with metabolic activity[49] can occur on the millisecond timescale. However, as shown in all cases, reducing the integration time inevitably decreases the signal-to-noise ratio, leading to image blurring and a loss of spatial resolution, which is analyzed based on the signal intensity distribution. To discuss the spatial resolution of images acquired on Ag wells (1s, integration time), **Figure 8** shows the profiles of Ag wells under three different scenarios, comparing non-covered wells with wells covered with phantoms exhibiting two different scattering powers. The PL images and corresponding photographs of the phantoms are shown along with the intensity profiles for each condition.

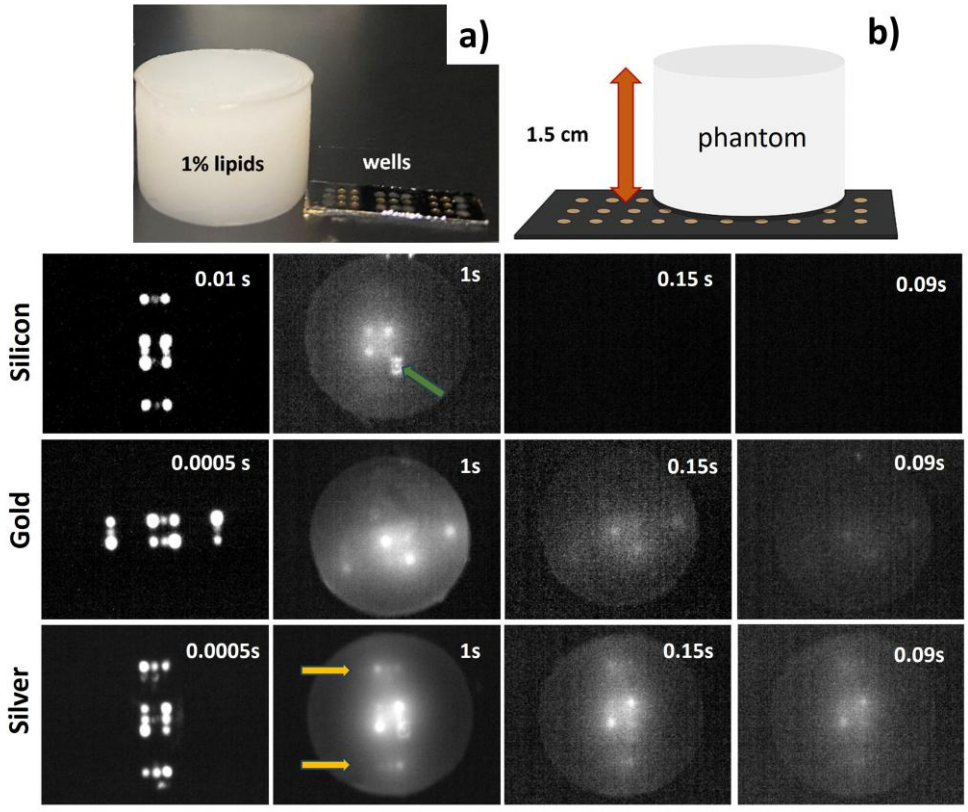


***Figure** 7. a-b) Description of the proof-of-concept imaging experiment, where the wells were placed below a 1.5 cm agar phantom mimicking tissue. NIR images of the covered wells on Si (top row), Au (middle row), and Ag (bottom row). All images were acquired under an irradiance of 15.8 mW/cm^2 and a wavelength of 808 nm. The integration time of the images is indicated in the corners of each image. As indicated by the yellow arrows (bottom row), fast and discernible signals were obtained for Ag under highly scattered media.*

Figure 8a presents the line profile extracted along the three spots marked in white in the top-center image. In the uncovered configuration, the profile exhibited three well-defined peaks corresponding to the three wells filled with NPs. The relative intensities of these peaks were in good agreement well with the expected emission strengths of the CSS, CS, and HU samples, yielding high, low, and intermediate maxima, respectively. Three wells, each 1 mm in diameter and separated by 500 μm, were clearly resolved, yielding an effective spatial resolution of approximately 400 μm according to the full width at half maximum (FWHM) of the derivative peaks (not shown). Therefore, the corresponding point-spread function (PSF) is on the order of 1 mm. As the scattering of the overlaying phantom increased, the contrast between the intensity maxima progressively decreased, reflecting a broadening of the PSF and a consequent loss of

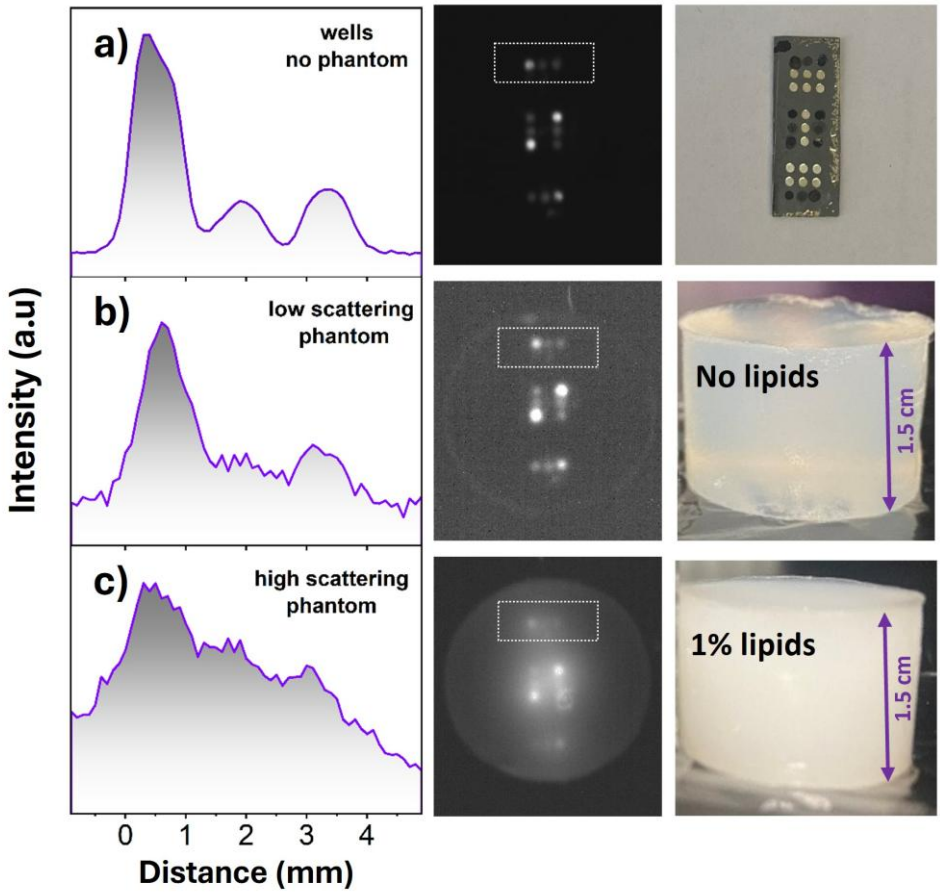


Figure 8. *Intensity profiles for a set of wells on Ag (a), the same wells under a phantom with moderate scattering (b) and high scattering (c) power. The profiles were obtained from a line crossing the three spots marked inside the rectangle in the PL images of the central column. The right column shows the uncovered set or wells and the phantoms used to extract the profile.*

spatial resolution. **Figure 8b** shows the same profile of the spots when a phantom with medium scattering power is placed on top, where a clear worsening is observed, but the spots are at the edge of discernibility. **Figure 8c** shows the profile when a phantom with high scattering power (the same as that used in Figure 7 containing 1% intralipids) was placed on top. In this case, the spots merged into diffuse emission regions extending over several millimeters, indicating that the PSF had expanded significantly. Although the individual emitters are no longer sharply separated, their collective pattern remains discernible, which is a remarkable result considering the strong scattering and defocusing conditions at the used depth. While the loss of spatial resolution is nearly one order of magnitude, the robust visibility of the emission features allows for the detection and localization of emitting regions even in the most blurred image under 1.5 cm of highly scattering media.

Conclusions

In this study, we demonstrate that the mirror effect of metallic substrates amplifies the effective photoluminescence emitted by micrometer-thick layers of Ag_2S-based nanoparticles deposited on them. Remarkably, this metal-assisted light extraction or substrate-mediated photoluminescence enhancement amplified the emitted signal in the biologically-relevant range. Furthermore, the enhanced photoluminescence signal allows photon extraction through a 1.5 cm depth of highly scattered media in fast acquisition times (90 ms) under mild excitation conditions (15.8 mW/cm^2). These results highlight the dual role of metals as optical mirrors and modulators of the thermal emission response for Ag_2S-based NPs, opening new promising route for improving bioimaging towards bio-integrated photonic thermometers.

Data availability

All the data generated and analyzed from this study are presented in the article and its Supplementary Information files. The data are also available from the corresponding author upon request. Source data are provided with this paper.

Acknowledgements

This work was done under the umbrella of the Severo Ochoa Centres of Excellence program through Grants CEX2020-001039-S and CEX2024-001445-S (MICIU/AEI/10.13039/501100011033). J. B also acknowledges Comunidad de Madrid for funding through the PIPF-2023/ECO-30481 fellowship. S.C, M.A and J.B acknowledge grants TED2021-131001A-I00 and CNS2022-135967 funded by MICIU/AEI/10.13039/501100011033 and by the European Union "NextGenerationEU"/PRTR, and grant PID2022-142525OA-I00 funded by MICIU/AEI/10.13039/501100011033 and by FEDER, EU.

Additional funding was provided by the Spanish Ministerio de Ciencia e Innovación MCIN/AEI/ 10.13039/501100011033 under projects PID2023-146775OB-I00 (INCLINA), PID2024-158675OB-C21, and the European Regional Development Fund ERDF, Grants CPP2021-008902, as well as CNS2023-145366 funded by MCIN/AEI/ 10.13039/501100011033 and by the "European Union NextGenerationEU/PRTR," by the Instituto de Salud Carlos III (PI24/01535), by the Comunidad Autónoma de Madrid (CAM) S2022/BMD-7403 RENIM-CM and TEC-2024COM-360 DISCO-6G grants and co-financed by the European structural and investment fund. D.H.O is grateful for Ramón y Cajal Fellowship RYC2022-036732-I funded by MCIN/AEI/ 10.13039/501100011033 and by "ESF investing in your future". BHJ and EMR acknowledges PID2023-151371OB-C21 and PID2023-151371OB-C22 by MCIN/AEI /10.13039/501100011033 and by FEDER, EU. PW thanks CSS for his scholarship no. 202304910071.C.M acknowledges PID2023-151946OB-I00,

References

1. Hong, G., Antaris, A. L. & Dai, H. Near-infrared fluorophores for biomedical imaging. *Nat. Biomed. Eng.* **1**, 0010 (2017).
2. Wang, F., Zhong, Y., Bruns, O., Liang, Y. & Dai, H. In vivo NIR-II fluorescence imaging for biology and medicine. *Nat. Photonics* **18**, 535–547 (2024).
3. Jaque, D. & Vetrone, F. Luminescence nanothermometry. *Nanoscale* **4**, 4301 (2012).

4. Zhou, J., del Rosal, B., Jaque, D., Uchiyama, S. & Jin, D. Advances and challenges for fluorescence nanothermometry. *Nat. Methods* **17**, 967–980 (2020).
5. Brites, C. D. S. *et al.* Spotlight on Luminescence Thermometry: Basics, Challenges, and Cutting-Edge Applications. *Adv. Mater.* **35**, 2302749 (2023).
6. Del Rosal, B. *et al.* In Vivo Contactless Brain Nanothermometry. *Adv. Funct. Mater.* **28**, 1806088 (2018).
7. Santos, H. D. A. *et al.* In Vivo Early Tumor Detection and Diagnosis by Infrared Luminescence Transient Nanothermometry. *Adv. Funct. Mater.* **28**, 1803924 (2018).
8. Ximendes, E. C. *et al.* In Vivo Ischemia Detection by Luminescent Nanothermometers. *Adv. Healthc. Mater.* **6**, 1601195 (2017).
9. Shen, Y. *et al.* Reliable and Remote Monitoring of Absolute Temperature during Liver Inflammation via Luminescence-Lifetime-Based Nanothermometry. *Adv. Mater.* **34**, 2107764 (2022).
10. Shen, Y. *et al.* Perspectives for Ag_2S NIR-II nanoparticles in biomedicine: from imaging to multifunctionality. *Nanoscale* **11**, 19251–19264 (2019).
11. Wang, P. *et al.* The role of temperature in the photoluminescence quantum yield (PLQY) of Ag2S-based nanocrystals. *Mater Horiz* (2024) doi:10.1039/D4MH01016G.
12. Gutierrez, I. Z. *et al.* Boosting the Near-Infrared Emission of Ag_2S Nanoparticles by a Controllable Surface Treatment for Bioimaging Applications. *ACS Appl. Mater. Interfaces* **14**, 4871–4881 (2022).
13. Santos, E. H. *et al.* Correction of spectral distortions in nanothermometry using machine learning. *Sens. Actuators Phys.* **389**, 116550 (2025).
14. Shen, Y., Lifante, J., Fernández, N., Jaque, D. & Ximendes, E. In Vivo Spectral Distortions of Infrared Luminescent Nanothermometers Compromise Their Reliability. *ACS Nano* **14**, 4122–4133 (2020).

15. Purcell, EM. Spontaneous emission probabilities at radio frequencies. *Phys. Rev.* **69**, 681 (1946).
16. Purcell, E. M., Torrey, H. C. & Pound, R. V. Resonance Absorption by Nuclear Magnetic Moments in a Solid. *Phys. Rev.* **69**, 37–38 (1946).
17. Drexhage, K. H., Kuhn, H. & Schäfer, F. P. Variation of the Fluorescence Decay Time of a Molecule in Front of a Mirror. *Berichte Bunsenges. Für Phys. Chem.* **72**, 329–329 (1968).
18. Geddes, C. D. & Lakowicz, J. R. Editorial: Metal-Enhanced Fluorescence. *J. Fluoresc.* **12**, 121–129 (2002).
19. Lakowicz, J. R. Radiative decay engineering 5: metal-enhanced fluorescence and plasmon emission. *Anal. Biochem.* **337**, 171–194 (2005).
20. Jeong, Y., Kook, Y.-M., Lee, K. & Koh, W.-G. Metal enhanced fluorescence (MEF) for biosensors: General approaches and a review of recent developments. *Biosens. Bioelectron.* **111**, 102–116 (2018).
21. Dasgupta, S. & Ray, K. Plasmon-enhanced fluorescence for biophotonics and bio-analytical applications. *Front. Chem.* **12**, 1407561 (2024).
22. Brolo, A. G. *et al.* Enhanced Fluorescence from Arrays of Nanoholes in a Gold Film. *J. Am. Chem. Soc.* **127**, 14936–14941 (2005).
23. Saboktakin, M. *et al.* Plasmonic Enhancement of Nanophosphor Upconversion Luminescence in Au Nanohole Arrays. *ACS Nano* **7**, 7186–7192 (2013).
24. Lu, D. *et al.* Plasmon Enhancement Mechanism for the Upconversion Processes in NaYF4:Yb3+,Er3+ Nanoparticles: Maxwell versus Förster. *ACS Nano* **8**, 7780–7792 (2014).
25. Molkenova, A., Choi, H. E., Park, J. M., Lee, J.-H. & Kim, K. S. Plasmon Modulated Upconversion Biosensors. *Biosensors* **13**, 306 (2023).

26. Moal, E. L. *et al.* Enhanced Fluorescence Cell Imaging with Metal-Coated Slides. *Biophys. J.* **92**, 2150–2161 (2007).
27. Guidelli, E. J., Ramos, A. P. & Baffa, O. Silver nanoparticle films for metal enhanced luminescence: Toward development of plasmonic radiation detectors for medical applications. *Sens. Actuators B Chem.* **224**, 248–255 (2016).
28. Lopez-Garcia, M. *et al.* Enhancement and Directionality of Spontaneous Emission in Hybrid Self-Assembled Photonic-Plasmonic Crystals. *SMALL* **6**, 1757–1761 (2010).
29. Molet, P. *et al.* Large area metasurfaces made with spherical silicon resonators. *NANOPHOTONICS* **9**, 943–951 (2020).
30. Song, J. *et al.* Large-area enhancement of far-field directional fluorescence emission using hybrid photonic crystal grating structure optimized by genetic algorithm. *Opt. Laser Technol.* **179**, 111319 (2024).
31. Yang, X. *et al.* Mirror-enhanced super-resolution microscopy. *Light Sci. Appl.* **5**, e16134–e16134 (2016).
32. Liu, Y. *et al.* On-Chip Mirror Enhanced Multiphoton Upconversion Super-Resolution Microscopy. *Nano Lett.* **23**, 5514–5519 (2023).
33. Nyman, M. *et al.* Large-area enhancement of far-field fluorescence intensity using planar nanostructures. *APL Photonics* **4**, 076101 (2019).
34. Vonk, S. J. W., van Swieten, T. P., Cocina, A. & Rabouw, F. T. Photonic Artifacts in Ratiometric Luminescence Nanothermometry. *Nano Lett.* **23**, 6560–6566 (2023).
35. Ruiz, D. *et al.* Ag/Ag2S Nanocrystals for High Sensitivity Near-Infrared Luminescence Nanothermometry. *Adv. Funct. Mater.* **27**, 1604629 (2017).
36. Coro, A. *et al.* Ag_2S Biocompatible Ensembles as Dual OCT Contrast Agents and NIR Ocular Imaging Probes. *Small* **19**, 2305026 (2023).
37. Ruiz, D. *et al.* Synthesis and characterization of Ag_2S and $Ag_2S/Ag_2(S,Se)$ NIR nanocrystals. *Nanoscale* **11**, 9194–9200 (2019).

38. Wang, P. *et al.* The role of temperature in the photoluminescence quantum yield (PLQY) of Ag_2 S-based nanocrystals. *Mater. Horiz.* **11**, 6158–6168 (2024).
39. Vega-Mayoral, V. *et al.* Exploring many-body phenomena: biexciton generation and auger recombination in Ag_2 S-based nanocrystals. *Nanoscale* **17**, 15697–15705 (2025).
40. De Wit, J. W. *et al.* New Insights in Luminescence and Quenching Mechanisms of Ag_2 S Nanocrystals through Temperature-Dependent Spectroscopy. *J. Phys. Chem. Lett.* **15**, 8420–8426 (2024).
41. Li, J. *et al.* Dual-Functional Nonmetallic Plasmonic Hybrids with Three-Order Enhanced Upconversion Emission and Photothermal Bio-Therapy. *Laser Photonics Rev.* **16**, 2200197 (2022).
42. Yeh, P. *Optical Waves in Layered Media*. (Wiley-Interscience, Hoboken, NJ, 2005).
43. Nasrallah, T. B., Dlala, H., Amlouk, M., Belgacem, S. & Bernède, J. C. Some physical investigations on Ag2S thin films prepared by sequential thermal evaporation. *Synth. Met.* **151**, 225–230 (2005).
44. Johnson, P. B. & Christy, R. W. Optical Constants of the Noble Metals. *Phys. Rev. B* **6**, 4370–4379 (1972).
45. Palik, E. D. *Handbook of Optical Constants of Solids*. (Academic press, Orlando San Diego New York, 1985).
46. Prasad, A. & Prasad, K. Effective permittivity of random composite media: A comparative study. *Phys. B Condens. Matter* **396**, 132–137 (2007).
47. Drexhage, K. H. Influence of a dielectric interface on fluorescence decay time. *J. Lumin.* **1–2**, 693–701 (1970).
48. Bueno, J., Jiménez-Solano, A., Anaya, M. & Carretero-Palacios, S. Plasmonic nanoparticles boost low-current perovskite LEDs governed by photon recycling effects. *RSC Adv.* **15**, 32497–32508 (2025).

49. Chrétien, D. *et al*. Mitochondria are physiologically maintained at close to 50 °C. *PLOS Biol*. **16**, e2003992 (2018).

Author contributions

B.H. Juarez proposed the concept and supervised the work. P. Wang, D. Carrica and A. Hernández Medel conducted synthesis and/or and characterization under the guidance of B.H. Juárez and E. Martin Rodriguez. J. Bueno, and S. Carretero performed simulations. A. Blanco and B. H. Juárez performed data analysis. C. Munuera performed KPFM experiments and analysis. M. Rodriguez Osorio performed the photolithographic wells. D. Granados and D. Jaque provided guidance. To the final version of the manuscript all authors contributed. The manuscript was supervised by B. H. Juárez.

Competing interests

The authors declare no competing interests.

Additional information

The online version contains supplementary material.

Supplementary Files

This is a list of supplementary files associated with this preprint. Click to download.

- Wangetal.SI.docx